Fuzzy-Immune-Regulated Adaptive Degree-of-Stability LQR for a Self-Balancing Robotic Mechanism: Design and HIL Realization

Omer Saleem, *Senior Member, IEEE*, Jamshed Iqbal, *Senior Member, IEEE*

***Abstract*—This letter formulates a fuzzy-immune adaptive system for the online adjustment of the Degree-of-Stability (DoS) of Linear-Quadratic-Regulator (LQR) procedure to strengthen the disturbance attenuation capacity of a self-balancing mechatronic system. The fuzzy-immune adaptive system uses pre-configured control input-based rules to alter the DoS parameter of LQR for dynamically relocating the closed-loop system's eigenvalues in the complex plane's left half. The corresponding changes in the eigenvalues are conveyed to the Riccati equation, which eventually yields the self-adjusting LQR gains. This arrangement allows for the flexible manipulation of the applied control effort and the response speed as the error conditions change. The efficacies of the self-tuning LQR scheme are verified by performing custom-designed hardware-in-the-loop experiments on the Quanser rotary inverted pendulum system. As compared to the DoS-LQR, the proposed controller improves the pendulum's transient recovery time, overshoots, input demands, and offsets by 32.3%, 50.5%, 33.9%, and 33.3%, respectively, under disturbances. These experimental outcomes verify that the proposed self-tuning LQR law considerably improves the system's disturbance attenuation capability.**

I. Introduction

Formulating control procedures for self-balancing robotic mechanisms has recently garnered a lot of attention [1]. Some of the notable real-world self-balancing control problems include the posture stabilization of bipedal exoskeletons [2], walking robots [3], two-wheeled transporters [4], etc. These systems rely upon the stabilization control principle of the inverted pendulum [5]. The Single-link Rotary-Inverted-Pendulum (SRIP) is a self-stabilizing robotic mechanism that is widely used to examine control algorithms for such systems [6]. It is an inherently under-actuated system with nonlinear dynamics and kinematic instability [7]. The SRIP balancing control problem becomes quite difficult to handle when the system is influenced by parametric uncertainties [8].

A plethora of agile control laws that deal with the aforesaid problem are proposed in the literature [9]. The proportional-integral-derivative controllers are reliable and simple, but, they lack the flexibility to robustly compensate for exogenous disturbances [10]. The fuzzy and neural controllers rely upon well-postulated logical rules and substantial training data to yield agile control effort, respectively [11, 12]. Despite their innate robustness, the sliding-mode-controllers repetitively switch between the sliding manifolds, which leads to disrupted control behavior and increases the chattering in the response [13, 14]. The Linear-Quadratic-Regulator (LQR) delivers optimal control effort [15]. However, it cannot robustly compensate for model variations, identification errors, and parametric uncertainties [16].

The prescribed Degree-of-Stability (DoS) LQR design robustifies the system's performance by reorganizing its closed-loop poles on the left side of the user-specified line $s = -\beta$ in the complex s-plane; where, "s" is the Laplace operator and $\beta \geq 0$ is a preset parameter that dictates the controller's DoS [17]. As compared to the conventional LQR, this augmentation reasonably improves the regulator's phase margin and aids in directing the applied control yield to improve the controller's robustness [18]. Unfortunately, this augmentation also makes the procedure sub-optimal by making a compromise between the disturbance-rejection capability and control input economy [19]. Due to design limitations, the fixed-gain DoS-LQR design is found to be inefficient in optimizing the control resource allocation as the error conditions change, especially under disturbances [20].

This letter contributes to addressing the aforesaid problem by developing a novel fuzzy-immune-regulated adaptive DoS-LQR for a self-balancing robotic system. The said control law is realized by employing the ubiquitous LQR with prescribed DoS as the baseline state compensator. The DoS-LQR is retrofitted with an auxiliary online adaptation law that modulates the parameter β, which in turn alters the solution of the Riccati equation to deliver self-tuning LQR gains. The salient contributions of this letter are presented as follows:

- Formulation of the novel self-adaptive DoS-LQR law.
- Synthesis of a bio-inspired self-tuning scheme that online adapts the DoS parameter β in LQR by using a pre-configured fuzzy immune system (FIS).
- Experimental validation of the proposed control law by performing customized hardware-in-the-loop (HIL) experiments on the Quanser SRIP platform [6].

The FIS is a bio-inspired computational paradigm that mimics the autonomous self-regulation behavior of the vertebrate immune system to alter the applied control stiffness to effectively reject the exogenous disturbances [21, 22]. It is realized by using a pre-calibrated two-input fuzzy inference system. Unlike other soft computing techniques (such as deep reinforcement learning [23]), the FIS requires relatively lesser computational resources while displaying good adaptability. The design and HIL realization of an FIS-regulated DoS-LQR law has never been discussed in the literature. Thus, this novel idea is the focal point of this letter.

Omer Saleem is with the National University of Computer and Emerging Sciences, Lahore, Pakistan (e-mail: omer.saleem@nu.edu.pk).

Jamshed Iqbal is with University of Hull, Hull, UK (corresponding author) phone: +44 1482 462187; e-mail: j.iqbal@hull.ac.uk).

The remaining letter is structured as follows: the mathematical model and the predetermined DoS-LQR design for the SRIP are presented in Section II. The proposed FIS-based adaptive DoS-LQR law is formulated in Section III. The HIL experiments and the corresponding results are analyzed in Section IV. The letter is concluded in Section V.

II. System Description

The SRIP platform is used to investigate the properties of the proposed control law. The schematic of an SRIP system is shown in Fig. 1. It is constructed by connecting the apparatus rod to a horizontal arm link that is rotated by a DC servo motor. The closed-loop feedback controller uses the system's states to generate appropriate control signals that are modulated to actuate the motor. The motor drives the horizontal arm to energize the rod and erect it. Once the rod erects itself, the balancing control law stabilizes it vertically. The rotary encoder attached to the motor's shaft measures the arm's angular position, denoted as α. The rotary encoder connected to the rod's pivoted end measures the rod's angular position, denoted as θ.

A. Mathematical Model

The Euler-Lagrange technique is used to formulate the system's dynamic model [24]. The system's Lagrangian is computed, as shown in (1), in terms of α, θ, $\dot{\alpha}$, and $\dot{\theta}$.

$$L = E_K - E_P \tag{1}$$

where, E_K and E_P are the system's kinetic and potential energies, respectively. The Lagrangian is given in (2), [24].

$$L = \frac{1}{2}\left(J_e + M_p r^2\right)(\dot{\alpha})^2 + \frac{1}{2}\left(M_p {l_p}^2 + J_p\right)\left(\dot{\theta}\right)^2 - M_p l_p r(\cos\theta)\dot{\alpha}\dot{\theta} - M_p l_p g(\cos\theta) \tag{2}$$

The Lagrangian is simplified by assuming that θ is always close to π rad. Without this assumption, the expression would include additional terms, in particular with J_p. The model parameters mentioned in (2) are listed in Table I [25]. The SRIP's equations of motion are derived as follows [24].

$$\frac{\delta}{\delta t}\left(\frac{\delta L}{\delta \dot{\alpha}}\right) - \frac{\delta L}{\delta \alpha} = \tau - b_v\dot{\alpha}, \qquad \frac{\delta}{\delta t}\left(\frac{\delta L}{\delta \dot{\theta}}\right) - \frac{\delta L}{\delta \theta} = 0 \tag{3}$$

where, τ is the motor's applied torque and b_v is the viscous friction in the DC motor. The friction is neglected in the model formulation. The torque is expressed in (4).

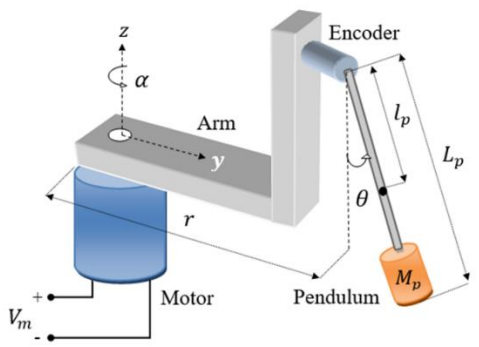

Fig. 1. Schematic representation of an SRIP system.

TABLE I
Model Parameters of the Quanser SRIP [25]

Symbol	Description	Value	Unit
M_p	Rod's mass	0.027	kg
l_p	Rod's center of mass	0.153	m
L_p	Rod's length	0.191	m
r	Arm's length	0.083	m
M_{arm}	Arm's mass	0.028	kg
g	Gravitational acceleration	9.810	m/s^2
J_e	Moment about shaft	1.23×10^{-4}	kgm^2
J_p	Moment about rod	1.10×10^{-4}	kgm^2
R_m	Motor's resistance	3.30	Ω
L_m	Motor's inductance	47.0	mH
K_t	Motor torque constant	0.028	Nm/A
K_m	Back EMF constant	0.028	Vs/rad
T_m	Maximum torque	0.14	Nm

$$\tau = \frac{K_t(V_m - K_m\dot{\alpha})}{R_m} \tag{4}$$

The torque is a function of the motor's input voltage V_m. The nonlinear equations, delivered by (3), are linearized about the vertical position; where, $\theta = \pi$ rad., $\alpha = 0$, $\dot{\theta} = 0$, $\dot{\alpha} = 0$. The linearized state equations are expressed in (5) and (6).

$$\ddot{\alpha} = \frac{1}{H}\left(rM_p^2 l_p^2 g\theta - \frac{\left(J_p + M_p l_p^2\right)K_t K_m}{R_m}\dot{\alpha} + \frac{\left(J_p + M_p l_p^2\right)K_t}{R_m}V_m\right) \tag{5}$$

$$\ddot{\theta} = \frac{1}{H}\left(M_p l_p g\left(J_e + M_p r^2\right)\theta - \frac{rM_p l_p K_t K_m}{R_m}\dot{\alpha} + \frac{rM_p l_p K_t}{R_m}V_m\right) \tag{6}$$

such that, $H = J_e J_p + M_p r^2 J_p + M_p l_p^2 J_e$

A linear system is represented in state space as,

$$\dot{x}(t) = \boldsymbol{A}x(t) + \boldsymbol{B}u(t), \qquad y(t) = \boldsymbol{C}x(t) + \boldsymbol{D}u(t) \tag{7}$$

where, $\boldsymbol{A}$ is the system matrix, $\boldsymbol{B}$ is the input matrix, $\boldsymbol{C}$ is the output matrix, $\boldsymbol{D}$ is the feed-forward matrix, and $y(t)$ is the output vector. The control vector $u(t)$ and state vector $x(t)$ of the SRIP system considered in this research are provided in (8), [6, 25].

$$u(t) = V_m(t), \quad x(t) = [\alpha(t) \quad \theta(t) \quad \dot{\alpha}(t) \quad \dot{\theta}(t)]^T \tag{8}$$

As per the equations in (5) and (6), the SRIP system is represented in the state space as given by Eq. 9, [25].

$$\boldsymbol{A} = \begin{bmatrix} 0 & 0 & 1 & 0 \\ 0 & 0 & 0 & 1 \\ 0 & a_1 & a_2 & 0 \\ 0 & a_3 & a_4 & 0 \end{bmatrix}, \quad \boldsymbol{B} = \begin{bmatrix} 0 \\ 0 \\ b_1 \\ b_2 \end{bmatrix}, \quad \boldsymbol{C} = \begin{bmatrix} 1 & 0 & 0 & 0 \\ 0 & 1 & 0 & 0 \\ 0 & 0 & 1 & 0 \\ 0 & 0 & 0 & 1 \end{bmatrix}, \quad \boldsymbol{D} = \begin{bmatrix} 0 \\ 0 \\ 0 \\ 0 \end{bmatrix} \tag{9}$$

where, $a_1 = \frac{rM_p^2 l_p^2 g}{H}$, $a_2 = \frac{-K_t K_m\left(J_p + M_p l_p^2\right)}{HR_m}$, $a_3 = \frac{M_p l_p g\left(J_e + M_p r^2\right)}{H}$, $a_4 = \frac{-rM_p l_p K_t K_m}{HR_m}$, $b_1 = \frac{K_t\left(J_p + M_p l_p^2\right)}{HR_m}$, $b_2 = \frac{rM_p l_p K_t}{HR_m}$.

B. Predetermined Degree-of-Stability LQR Design

To realize the DoS-LQR, the LQR's conventional Quadratic-Cost-Function (QCF) is restructured to reposition the eigenvalues of the system matrix $\boldsymbol{A}$ on the left side of the line prescribed as $s = -\beta$ in the s-plane, where β is a predetermined positive parameter [26]. The relocation of the system's eigenvalues on the left side of $s = -\beta$ ensures that the poles are always restricted within the complex plane's left

half. This arrangement guarantees the closed-loop stability of the control law. To realize the DoS-LQR, the conventional QCF is altered by assigning an exponential variable, $e^{2\beta t}$, to it. The altered QCF is expressed below [17].

$$J_{dos} = \frac{1}{2}\int_0^\infty e^{2\beta t}[x(t)^T \boldsymbol{Q} x(t) + u(t)^T \boldsymbol{R} u(t)]\, dt \quad (10)$$

where, $\boldsymbol{Q} \in \mathbb{R}^{4\times4}$ and $\boldsymbol{R} \in \mathbb{R}$ are the state and control weighting matrices, respectively. They are selected such that $\boldsymbol{Q} = \boldsymbol{Q}^T \geq 0$ and $\boldsymbol{R} = \boldsymbol{R}^T > 0$. The policy employed to tune the matrices $\boldsymbol{Q}$ and $\boldsymbol{R}$ is discussed in the next subsection. The QCF J_{dos} can be simplified as shown in (11).

$$J_{dos} = \frac{1}{2}\int_0^\infty [p(t)^T \boldsymbol{Q} p(t) + c(t)^T \boldsymbol{R} c(t)]\, dt \quad (11)$$

where, $p(t) = e^{\beta t}x(t), \quad c(t) = e^{\beta t}u(t)$

where, $p(t)$ is the altered state vector and $c(t)$ is the altered input vector. The derivative of $p(t)$ is expressed in (12).

$$\dot{p}(t) = e^{\beta t}\dot{x}(t) + \beta e^{\beta t}x(t) \quad (12)$$

By replacing $\dot{x}(t)$ with its expression mentioned in Eq. 7, along with other suitable substitutions, the system's altered state equation, $\dot{p}(t)$, is expressed below [17].

$$\dot{p}(t) = (\boldsymbol{A} + \beta \boldsymbol{I})p(t) + \boldsymbol{B}c(t) \quad (13)$$

where, I represents an identity matrix of order 4×4. The updated system matrix modifies the Riccati equation's expression as shown in (14).

$$(\boldsymbol{A} + \beta \boldsymbol{I})^T \boldsymbol{P} + \boldsymbol{P}(\boldsymbol{A} + \beta \boldsymbol{I}) - \boldsymbol{P}\boldsymbol{B}\boldsymbol{R}^{-1}\boldsymbol{B}^T\boldsymbol{P} + \boldsymbol{Q} = 0 \quad (14)$$

The symmetric positive-definite matrix $\boldsymbol{P} \in \mathbb{R}^{4\times4}$ is the Riccati equation's solution. Retrofitting the QCF with $e^{2\beta t}$ mutates the original system matrix $\boldsymbol{A}$ into $\boldsymbol{A} + \beta \boldsymbol{I}$, which changes the position of the system's eigenvalues depending on the prescribed value of β. Hence, the matrix $\boldsymbol{P}$ depends on the prescribed value of β. This solution is utilized to compute the LQR gain vector $\boldsymbol{K}$, as shown in (15).

$$\boldsymbol{K} = \boldsymbol{R}^{-1}\boldsymbol{B}^T\boldsymbol{P} \quad (15)$$

The gain vector $\boldsymbol{K}$ is also indirectly influenced by β. The DoS-LQR is realized by introducing the offset $\beta \boldsymbol{I}$ in the original matrix $\boldsymbol{A}$. The DoS-LQR law is expressed below.

$$u_{dos}(t) = -\boldsymbol{K}x(t) \quad (16)$$

The stability of the DoS-LQR is proven via the following Lyapunov function.

$$V(t) = p(t)^T \boldsymbol{P}(t) p(t) > 0, \quad \text{for } p(t) \neq 0 \quad (17)$$

The first derivative of $V(t)$ is derived as follows [16].

$$\begin{aligned}\dot{V}(t) &= 2p(t)^T \boldsymbol{P}\dot{p}(t) \quad (18)\\ &= p(t)^T\big((\boldsymbol{A} + \beta \boldsymbol{I})^T\boldsymbol{P} + \boldsymbol{P}(\boldsymbol{A} + \beta \boldsymbol{I})\big)p(t)\\ &\quad - 2p(t)^T(\boldsymbol{P}\boldsymbol{B}\boldsymbol{R}^{-1}\boldsymbol{B}^T\boldsymbol{P})p(t)\end{aligned}$$

By substituting equation (14) in (18), $\dot{V}(t)$ is simplified as shown in below.

$$\dot{V}(t) = -p(t)^T \boldsymbol{Q} p(t) - p(t)^T(\boldsymbol{P}\boldsymbol{B}\boldsymbol{R}^{-1}\boldsymbol{B}^T\boldsymbol{P})p(t) \quad (19)$$

The expression of $\dot{V}(t) < 0$ if $\beta \geq 0$, $\boldsymbol{Q} = \boldsymbol{Q}^T \geq 0$, and $\boldsymbol{R} = \boldsymbol{R}^T > 0$. These specifications ensure the closed-loop convergence of the DoS-LQR scheme.

C. Controller Parameter Tuning

The controller parameters are optimized offline by minimizing the cost function expressed in (20).

$$J_e = \int_0^{\mathrm{T}} |\varepsilon_\alpha(t)|^2 + |\varepsilon_\theta(t)|^2 + |u(t)|^2 dt \quad (20)$$

where, $\varepsilon_\alpha(t)$ and $\varepsilon_\theta(t)$ represent the state error variables. They are evaluated as $\varepsilon_\alpha(t) = \alpha(0) - \alpha(t)$ and $\varepsilon_\theta(t) = \pi - \theta(t)$. The function J_e asserts an equal weight upon the error and input minimization criteria for an optimal control yield [27]. The weighting coefficients are selected from the range [0, 100] and β is selected from the range [0, 10]. The flow chart of the parameter tuning algorithm is depicted in Fig. 2. The tuning is begun with $\boldsymbol{Q} = diag(1 \quad 1 \quad 1 \quad 1)$, $\boldsymbol{R} = 1$, and $\beta = 0.01$. The experimental trials for parameter tuning are conducted via the procedure discussed in Section IV. In every trial, the parameters are updated appropriately, the SRIP's rod is manually erected, and balanced for 10.0 sec. to compute the resulting cost $J_{e,k}$; where, k is the trial number. The algorithm explores the search space in the direction of the gradient-descent of J_e to ensure that the cost is decreasing as the exploration progresses. If the present cost ($J_{e,k}$) is lesser than the cost of the previous trial ($J_{e,k-1}$), the local minimum-cost variable $J_{e,min}$ is updated. The search is terminated if either $J_{e,min}$ achieves the user-specified threshold value or the maximum number of trials k_{max} are completed. In this work, the user-specified threshold for $J_{e,min}$ is set at 1.0×10^4 and $k_{max} = 30$. These settings are decided as per the expert's experience. The tuned parameters are $\boldsymbol{Q} = diag(38.2 \quad 52.6 \quad 5.3 \quad 2.1)$, $\boldsymbol{R} = 1.02$, and $\beta = 0.516$. The LQR gains are computed as $\boldsymbol{K} = [-8.79 \quad 158.16 \quad -5.51 \quad 21.73]$.

III. Proposed Control Methodology

The parameter β is adaptively tuned to formulate the proposed adaptive DoS-LQR [18, 20].

A. Adaptive DoS-based LQR Law

The online adaptation of β repositions the eigenvalues on the left side of the self-adjusting line $s = -\beta(t)$. The cost function in (10) is incorporated with $\beta(t)$ instead of fixed β. Correspondingly, the Riccati equation in (14) is also modified by replacing β with $\beta(t)$ [26]. The updated solution $\boldsymbol{P}(t)$ then delivers the self-adjusting LQR gains as shown in (21).

$$\boldsymbol{K}(t) = \boldsymbol{R}^{-1}\boldsymbol{B}^T\boldsymbol{P}(t) \quad (21)$$

The adaptive DoS-LQR law is expressed below [20].

$$u'(t) = -\boldsymbol{K}(t)x(t) \quad (22)$$

The online adaptation of β is done via FIS. The proposed FIS-regulated adaptive DoS-LQR law is shown in Fig. 3.

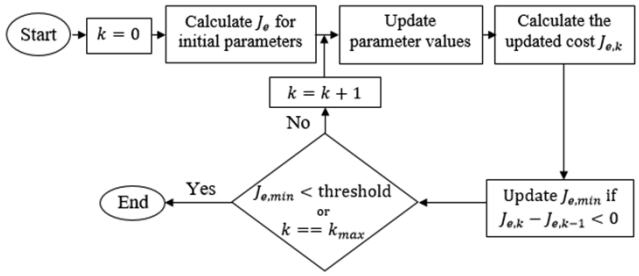

Fig. 2. Flow diagram of the parameter tuning algorithm

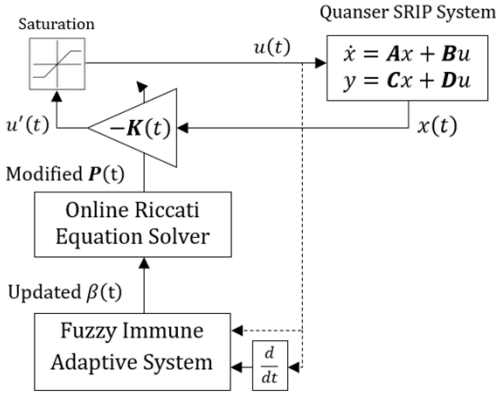

Fig. 3. Proposed adaptive DoS-LQR procedure

B. Fuzzy-Immune Self-Adaptation Law

The FIS is an intelligent information processing system that self-regulates the system's immune response to enhance its adaptability and response speed to effectively reject the disturbance [28]. The biological immune system contains antibody molecules and lymphocytes [29]. Altogether, the helper T cells (T_H cells), the suppressor T cells (T_S cells), and the B cells contribute to reproducing the lymphocytes. The B cells estimate the extent of the foreign attacking antigens. Upon determination, the B-cells activate an appropriate concentration of T_H cells to produce plasma cells, which in turn produce antibodies to reciprocate the attack. As the antigen assault becomes weak, the T_S cells are triggered to inhibit the creation of antibodies. The successive activation and inhibition of the antibody-production process is adaptively regulated by the T_S and T_H cells working together. This self-regulatory behavior flexibly modulates the system's damping against foreign attacks and ensures a fast transient response. The total concentration of B cells generated in this cycle is computed as shown below [21].

$$v(n) = T_H(n) - T_S(n) \tag{23}$$

where, $T_H(n) = \rho\, d(n), \quad T_S(n) = \rho\, \lambda\, m\big(v(n), \dot{v}(n)\big) d(n)$

such that, $v(n)$ is B cell stimulus (or concentration) at n^{th} generation, $T_H(n)$ is the T_H cells concentration, $T_S(n)$ is the T_S cells concentration, $d(n)$ is the antigen concentration, $m(.)$ is a nonlinear stimulus-suppression function that adaptively modulates the suppression rate of antibody production, ρ is the preset positive stimulation factor, and λ is the preset positive suppression factor. The B cell stimulus is expressed in (24), [22, 29].

$$v(n) = \rho\left(1 - \lambda\, m\big(v(n), \dot{v}(n)\big)\right) d(n) \tag{24}$$

Similar to biological systems, the physical systems also get degraded by random disturbances. Hence, in this work, an FIS is formulated to effectively manipulates the applied stimulation. The following map presents one-to-one correspondence between a biological and SRIP system [22].

Biological system		**Physical system**
Immune system	→	SRIP system
Antibody generation, n	→	Sampling interval, t
Antigen concentration, $d(n)$	→	Error variable, $e(t)$
B-cell stimulation, $v(n)$	→	Control input, $u(t)$

This map yields the immune feedback control law in (25).

$$u(t) = f(t)e(t) \tag{25}$$

This control law depends on the classical error $e(t)$ and an artificial-immune gain-adaptation law expressed as $f(t) = \rho\big(1 - \lambda\, m(u, \dot{u})\big)$. In this work, the stimulus-suppression function $m(.)$ is implemented via the FIS [29]. The variables $u(t)$ and $\dot{u}(t)$ are treated as the inputs, whereas, $m(u, \dot{u})$ is the output of the FIS. Seven linguistic variables, designated as Negative-Big (NB), Negative-Medium (NM), Negative-Small (NS), Zero (Z), Positive-Small (PS), Positive-Medium (PM), and Positive-Big (PB) are used to define the inputs and output variables. The input and the output variables are normalized within the range [-1, 1] a priori. Table II represents the fuzzy rules to construct the function $m(.)$. The fuzzy implication is done via the Mamdani inference (max-min) method as shown in (26).

$$\mu_{ij} = min\left(h_{i1}(u), h_{j2}(\dot{u})\right) \tag{26}$$

where, μ is the Membership Function's (MF's) degree and $h_{ij}(.)$ is the triangular-shaped MF of the following form.

$$h_{ij}(g) = \begin{cases} 1 + \dfrac{g - c_{ij}}{b_{i,j}^{-}}, & -b_{ij}{}^{-} \le g - c_{ij} \le 0 \\ 1 - \dfrac{g - c_{ij}}{b_{ij}{}^{+}}, & 0 \le g - c_{ij} \le b_{ij}{}^{+} \\ 0, & otherwise \end{cases} \tag{27}$$

where, g is the normalized input u or $\dot{u}$, and $b_{ij}{}^{+}$, c_{ij}, and $b_{ij}{}^{-}$ are the right-half width, centroid, and left-half width of the j^{th} input MF of the i^{th} input, respectively. Apart from being computationally simple to implement and having an intuitive interpretation, the usage of asymmetrical triangular MFs increases the controller's design flexibility. The input and output MF waveforms are shown in Fig. 4. The decisions are de-fuzzified via the center-of-gravity method to evaluate the crisp output $m(u, \dot{u})$ as shown in (28).

$$m(u, \dot{u}) = \frac{\sum_{i=1}^{7}\sum_{j=1}^{7}\big(\mu_{ij} \times w_{ij}\big)}{\sum_{i=1}^{7}\sum_{j=1}^{7}\mu_{ij}} \tag{28}$$

where, w is the centroid of the output MF. The updated values of function $m(u, \dot{u})$ are used to compute $\beta(t)$. The formulation of the adaptive DoS $\beta(t)$ is expressed in (29).

$$\beta(t) = \rho\big(1 - \lambda\, m(u, \dot{u})\big) \tag{29}$$

The parameters λ and ρ are selected from the range [0, 10] via the tuning procedure prescribed in Section II (C). The selected parameter values are $\lambda = 0.645$ and $\rho = 0.812$. The updated values of β yielded by (29) modify $\boldsymbol{P}(t)$ to deliver the self-tuning vector $\boldsymbol{K}(t)$ as shown in (21), (See Fig. 3).

TABLE II
RULE BASE TO CONSTRUCT THE STIMULUS SUPPRESSION FUNCTION

$m(u, \dot{u})$	$\dot{u}$						
u	NB	NM	NS	Z	PS	PM	PB
NB	PB	PB	PM	PM	PS	PS	Z
NM	PB	PM	PM	PS	PS	Z	NS
NS	PM	PM	PS	PS	Z	NS	NS
Z	PM	PS	PS	Z	NS	NS	NM
PS	PS	PS	Z	NS	NS	NM	NM
PM	PS	Z	NS	NS	NM	NM	NB
PB	Z	NS	NS	NM	NM	NB	NB

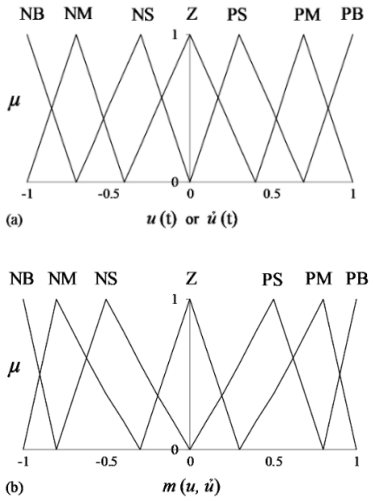

Fig. 4. (a) Input MFs of the FIS, (b) Output MFs of the FIS.

The parameter settings in (29) ensure $\beta(t) \geq 0$ to maintain the controller's asymptotic stability. The FIS uses control input-driven immune adaptation rules to increase β under large error (disturbance) conditions to yield a stiff control effort. Conversely, it reduces β under small error (equilibrium) conditions to apply a mild control effort. Hence, this way, the robustness and adaptability of the LQR method are improved to efficiently reject the disturbances while economizing the overall control energy expenditure. The Immune-adaptive DoS-LQR is referred to as "IDoS-LQR".

IV. Results and Discussions

The HIL experiments used to analyze the performance of the DoS-LQR and IDoS-LQR are presented below.

A. Experimental Setup

The HIL experiments are performed on the Quanser SRIP setup shown in Fig. 5. The encoder measurements are acquired at a sampling rate of 1.0 kHz by the NI-ELVIS DAQ board. This data is serially communicated to the control software at 9600 bps. The customized control application is developed by using the LabVIEW software, which is operated on an embedded computer with a 2.1 GHz, 64-bit microprocessor, and 8.0 GB RAM. The application's front end serves to graphically display the state and control variations in real time. The control software bounds the computed control signals within ±18.0 V (motor's rated voltage) via a saturation function to prevent the actuator from overheating (See Fig. 3). The resulting control signals are serially communicated to the onboard motor driver circuit that amplifies them to drive the motor and stabilize the SRIP.

B. HIL Experiments and Results

The efficacy of each controller is characterized by conducting the following experiments. In each experiment, the rod is erected and allowed to balance vertically while the arm tracks the reference station. To facilitate the data visualization, the graph plots are displayed in degrees.

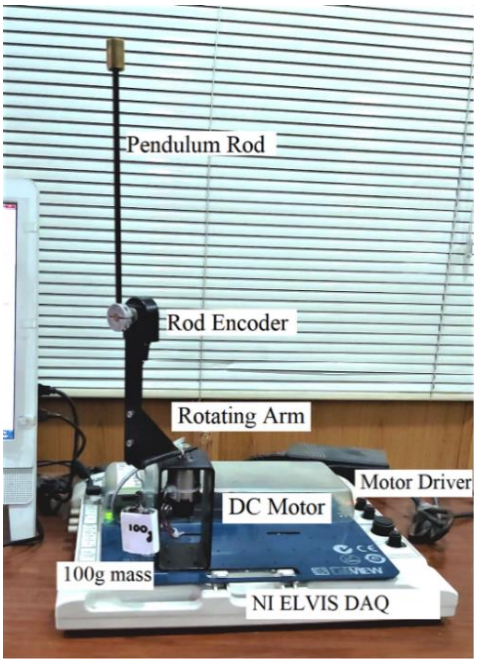

Fig. 5. Quanser SRIP setup.

1. *Position regulation*: This experiment assesses the reference-tracking capability of the arm while stabilizing the rod in the vertical position under disturbance-free conditions. The responses of $\alpha(t)$, $\theta(t)$, $V_m(t)$, $\beta(t)$ and $\boldsymbol{K}(t)$ are depicted in Fig. 6.
2. *Impulse disturbance attenuation*: This experiment investigates the controller's resilience against impulsive forces by administering a pulse signal of -5.0 V peak and 100 msec. duration in $V_m(t)$ at discrete intervals. The variations in $\alpha(t)$, $\theta(t)$, $V_m(t)$, $\beta(t)$ and $\boldsymbol{K}(t)$ are illustrated in Fig. 7.
3. *Step disturbance rejection*: This experiment analyzes the controller's immunity against load-torque changes by injecting a simulated step signal of -5.0 V in the control signal at t ≈ 7.5 sec. The responses of $\alpha(t)$, $\theta(t)$, $V_m(t)$, $\beta(t)$ and $\boldsymbol{K}(t)$ are shown in Fig. 8.
4. *High frequency disturbance suppression*: This experiment analyzes the controller's robustness against mechanical and sensor noise by introducing a simulated sinusoidal signal, $\mathrm{d(t)} = \sin(20\pi\mathrm{t})$, in V_m. The variations in $\alpha(t)$, $\theta(t)$, $V_m(t)$, $\beta(t)$ and $\boldsymbol{K}(t)$ are shown in Fig. 9.
5. *Low frequency disturbance suppression*: This experiment analyzes the controller's robustness against low frequency disturbances by injecting a simulated sinusoidal signal, $\mathrm{d(t)} = \sin(2\pi\mathrm{t})$, in V_m. The variations in $\alpha(t)$, $\theta(t)$, $V_m(t)$, $\beta(t)$ and $\boldsymbol{K}(t)$ are shown in Fig. 10.
6. *Model variation compensation*: This experiment analyzes the controller's resilience against the model variations by attaching a 0.1 kg mass underneath the pendulum's rod-arm assembly, at t ≈ 4.0 sec, as shown in Fig. 4. The consequent alteration in the system's model leads to state deviations. The variations in $\alpha(t)$, $\theta(t)$, $V_m(t)$, $\beta(t)$ and $\boldsymbol{K}(t)$ are shown in Fig. 11.

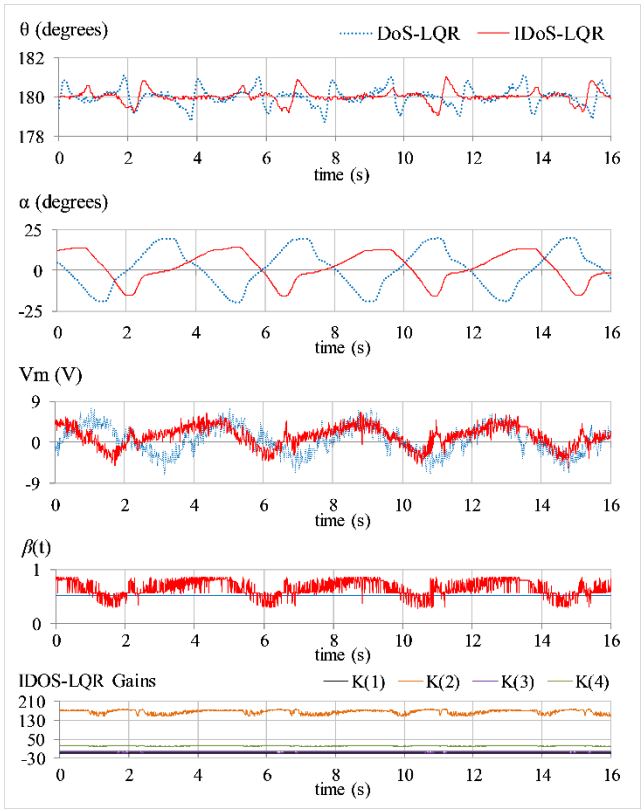

Fig. 6. SRIP's behavior under normal conditions.

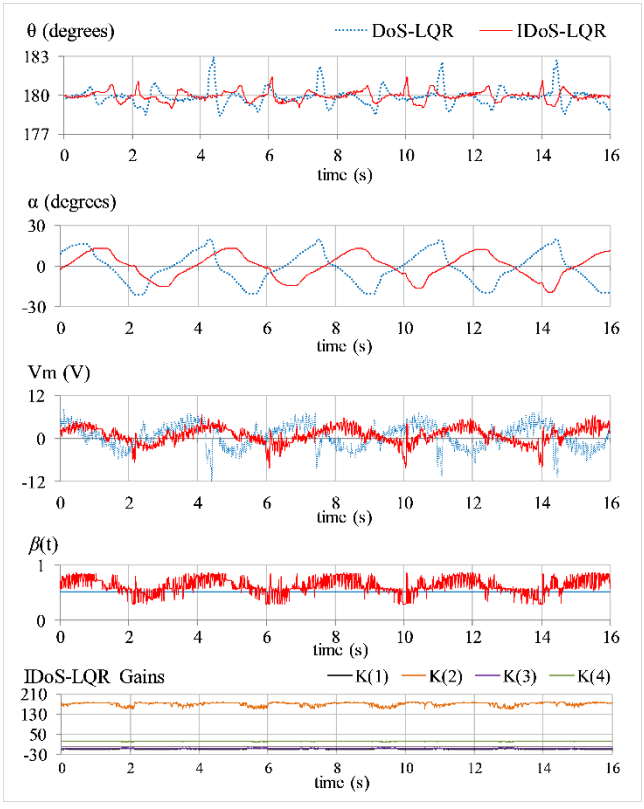

Fig. 7. SRIP's behavior under impulse disturbances.

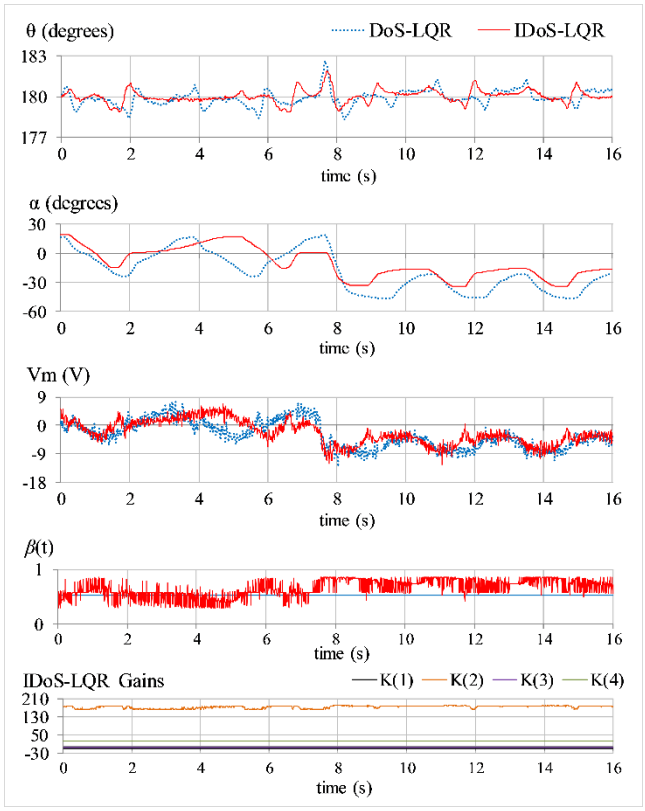

Fig. 8. SRIP's behavior under step disturbance.

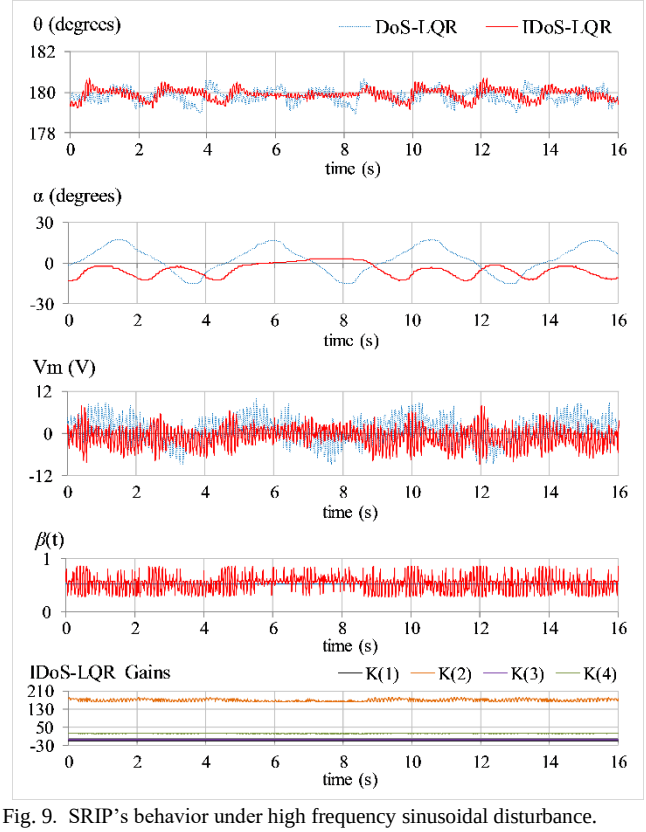

Fig. 9. SRIP's behavior under high frequency sinusoidal disturbance.

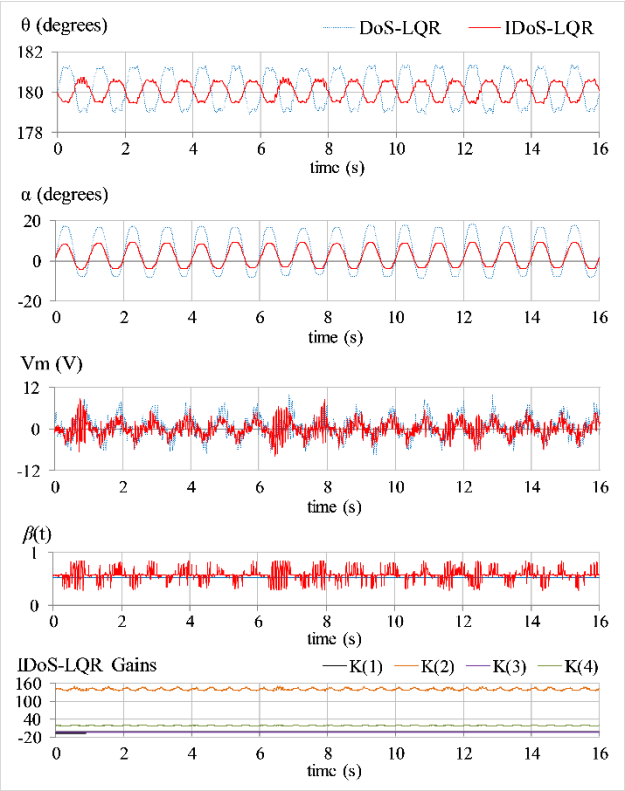

Fig. 10. SRIP's behavior under low frequency sinusoidal disturbance.

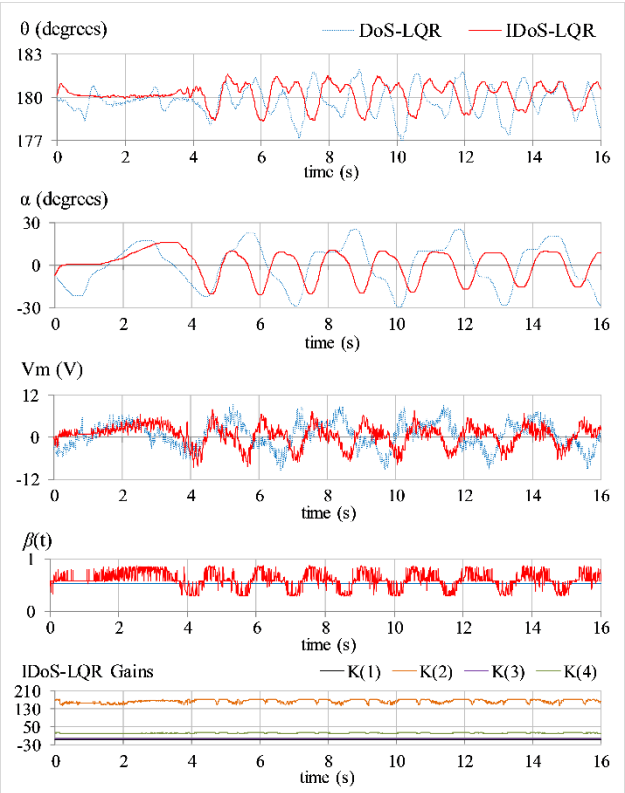

Fig. 11. SRIP's behavior under model variation.

C. *Comparative Analysis and Discussions*

The experimental outcomes are assessed as per the following Performance Metrics (PMs): the root-mean-square-error (e_{x_RMS}) in the SRIP states, the rod's duration of recovery ($t_{s,\theta}$) after a transient disturbance, the absolute peak of disturbance-induced overshoot ($|M_{p,x}|$) in the rod, the post-disturbance offset (α_{off}) in the arm's position, the peak-to-peak amplitude ($\alpha_{p\text{-}p}$) of post-disturbance oscillations in the arm., the mean-squared value of motor voltage (MSV_m), the peak motor voltage (V_p) under disturbance conditions [30]. These PMs are used to compare IDoS-LQR with DoS-LQR. The experimental results are quantified in Table III, along with the relative performance improvement contributed by IDoS-LQR as compared to DoS-LQR. In **Experiment 1**, the IDoS-LQR surpasses DoS-LQR by yielding optimum position regulation behavior and control input economy. In **Experiment 2**, the IDoS-LQR exhibits a relatively faster transit speed than DoS-LQR with strong damping against the overshoots while curbing the control energy demands. In **Experiment 3**, the IDoS-LQR outperforms DoS-LQR by effectively minimizing α_{off} and $\alpha_{p\text{-}p}$ while preserving the input economy. In **Experiments 4** and **5**, the IDoS-LQR effectively attenuates the sinusoidal disturbances by minimizing the position regulation errors, chattering content, and control energy demands. In **Experiment 6**, the IDoS-LQR attenuates the fluctuations while ensuring an economical control activity. The rapid variations in $\beta(t)$ and the IDoS-LQR gains improve the controller's robustness to reject the disturbances. The analysis authenticates the enhanced adaptability of the IDoS-LQR scheme against disturbances as compared to DoS-LQR. Unlike the schemes presented in [28-30], the IDoS-LQR adjusts a single parameter β to modify the LQR gains, which simplifies its realization while upholding its robustness.

TABLE III
SUMMARY OF EXPERIMENTAL RESULTS

Experiment	PM		Control Law		Improvement (%)
	Symbol	Units	DoS-LQR	IDoS-LQR	
1	e_{θ_RMS}	deg.	0.42	0.29	30.95
	e_{α_RMS}	deg.	12.24	9.28	24.18
	MSV_m	V^2	9.10	7.08	22.20
2	e_{θ_RMS}	deg.	0.63	0.37	41.27
	$\|M_{p,\theta}\|$	deg.	2.97	1.47	50.51
	$t_{s,\theta}$	sec.	0.68	0.46	32.35
	e_{α_RMS}	deg.	11.75	8.92	24.08
	MSV_m	V^2	10.78	6.31	41.47
	V_p	V	-12.30	-8.13	33.90
3	e_{θ_RMS}	deg.	0.57	0.45	21.05
	e_{α_RMS}	deg.	28.07	17.43	37.07
	α_{off}	deg.	-34.50	-23.00	33.33
	$\alpha_{p\text{-}p}$	deg.	24.55	18.65	24.03
	MSV_m	V^2	29.12	18.10	37.84
	V_p	V	-12.98	-12.28	5.39
4	e_{θ_RMS}	deg.	0.43	0.29	32.56
	e_{α_RMS}	deg.	9.90	6.85	30.80
	MSV_m	V^2	12.99	9.07	30.18
5	e_{θ_RMS}	deg.	0.82	0.49	40.24
	e_{α_RMS}	deg.	10.45	6.68	36.07
	MSV_m	V^2	9.11	5.77	30.66
6	e_{θ_RMS}	deg.	0.93	0.75	19.35
	e_{α_RMS}	deg.	14.80	9.94	32.84
	MSV_m	V^2	12.88	8.49	34.08

V. Conclusion

This article uses FIS to formulate an innovative self-tuning DoS-LQR method to strengthen the disturbance rejection capacity of self-balancing robotic systems. The FIS bridges the gap between immunology and engineering by mathematically modeling the immune system. It uses the system's input variations to enhance the controller's adaptability. The results validate that the IDoS-LQR offers superior robustness, economical control activity, and closed-loop stability. The IDoS-LQR procedure can be extended to other systems if the state-space model and the customized $\beta(t)$ function of the new system are available a priori. However, the proposed scheme will not perform as effectively as desired if the customized $\beta(t)$ function is ill-calibrated or if the system's state-space model contains modeling and identification errors. In the future, the implications of reinforcement learning can be analyzed to self-adjust β. Furthermore, the IDoS-LQR can be compared with other self-tuning LQR methods to assess its potential shortcomings.

References

[1] X. Gao, L. Yan, Z. He, G. Wang and I. -M. Chen, "Design and Modeling of a Dual-Ball Self-Balancing Robot," *IEEE Robot. Autom. Lett.*, vol. 7, no. 4, pp. 12491-12498, Oct. 2022.

[2] A. F. Soliman and B. Ugurlu, "Robust Locomotion Control of a Self-Balancing and Underactuated Bipedal Exoskeleton: Task Prioritization and Feedback Control," *IEEE Robot. Autom. Lett.*, vol. 6, no. 3, pp. 5626-5633, Jul. 2021.

[3] L. Patnaik, L. Umanand, "Physical constraints, fundamental limits, and optimal locus of operating points for an inverted pendulum based actuated dynamic walker," *Bioinspir. Biomim.*, vol. 10, no. 6, 064001, Oct. 2015.

[4] M. Moness, D. Mahmoud, A. Hussein, "Real-time Mamdani-like fuzzy and fusion-based fuzzy controllers for balancing two-wheeled inverted pendulum," *J. Ambient Intell. Human. Comput.* vol. 13, pp. 3577–3593, Jul. 2022.

[5] H. Chen, B. Wang, Z. Hong, C. Shen, P. M. Wensing and W. Zhang, "Underactuated Motion Planning and Control for Jumping With Wheeled-Bipedal Robots," *IEEE Robot. Autom. Lett*,, vol. 6, no. 2, pp. 747-754, Apr. 2021.

[6] O. Saleem, J. Iqbal, M.S. Afzal, "A robust variable-structure LQI controller for under-actuated systems via flexible online adaptation of performance-index weights," Plos one, vol. 18, no. 3, e0283079, Mar. 2023.

[7] H. Chen, P. M. Wensing and W. Zhang, "Optimal Control of a Differentially Flat Two-Dimensional Spring-Loaded Inverted Pendulum Model," *IEEE Robot. Autom. Lett.*, vol. 5, no. 2, pp. 307-314, Apr. 2020.

[8] H. Gritli, S. Belghit, "Robust feedback control of the underactuated Inertia Wheel Inverted Pendulum under parametric uncertainties and subject to external disturbances: LMI formulation," *J. Franklin Inst.*, vol. 355, no. 18, pp. 9150-9191, Dec. 2018.

[9] I. Koryakovskiy, M. Kudruss, R. Babuška, W. Caarls, C. Kirches, K. Mombaur, J. P. Schlöder, H. Vallery, "Benchmarking model-free and model-based optimal control," *Robot. Auton. Syst.*, vol. 92, pp. 81-90, Jun. 2017.

[10] M. Keppler, C. Raschel, D. Wandinger, A. Stemmer and C. Ott, "Robust Stabilization of Elastic Joint Robots by ESP and PID Control: Theory and Experiments," *IEEE Robot. Autom. Lett.*, vol. 7, no. 3, pp. 8283-8290, Jul. 2022

[11] O. S. Bhatti, O. B. Tariq, A. Manzar, O. A. Khan, "Adaptive intelligent cascade control of a ball-riding robot for optimal balancing and station-keeping," *Adv. Robot.*, vol. 32, no. 2, pp. 63-76, 2018.

[12] M. B. Anjum, Q. Khan, S. Ullah, G. Hafeez, A. Fida, J. Iqbal, F. R. Albogamy, "Maximum Power Extraction from a Standalone Photo Voltaic System via Neuro-Adaptive Arbitrary Order Sliding Mode Control Strategy with High Gain Differentiation," *Appl. Sci.*, vol. 12, no. 6, 2773, 2022.

[13] S. Ahmad, A. A. Uppal, M. R. Azam, J. Iqbal, "Chattering Free Sliding Mode Control and State Dependent Kalman Filter Design for Underground Gasification Energy Conversion Process," *Electronics*, vol. 12, no. 4, 876, 2023.

[14] M. Ghafarian, B. Shirinzadeh, A. Al-Jodah and T. K. Das, "Adaptive Fuzzy Sliding Mode Control for High-Precision Motion Tracking of a Multi-DOF Micro/Nano Manipulator," *IEEE Robot. Autom. Lett.*, vol. 5, no. 3, pp. 4313-4320, Jul. 2020.

[15] V. Klemm et al., "LQR-Assisted Whole-Body Control of a Wheeled Bipedal Robot With Kinematic Loops," *IEEE Robot. Autom. Lett.*, vol. 5, no. 2, pp. 3745-3752, Apr. 2020.

[16] O. Saleem, F. Abbas, J. Iqbal, "Complex Fractional-Order LQIR for Inverted-Pendulum-Type Robotic Mechanisms: Design and Experimental Validation," *Mathematics*, vol. 11, no. 4, 913, 2023.

[17] D. Xue, Y. Q. Chen, D. P. Atherton, *Linear Feedback Control: Analysis and Design with MATLAB.* Philadelphia, USA: SIAM, 2007.

[18] S. M. Azimi, R. A. Naghizadeh, A. R. Kian, "Optimal Controller Design for Interconnected Power Networks with Predetermined Degree of Stability," *IEEE Syst. J.*, vol. 13, no. 3, pp. 3165-3175, Sep. 2019.

[19] V. Radisavljevic, S. Koskie, "Suboptimal strategy for the finite-time linear-quadratic optimal control problem," *IET Control Theory Appl*, vol. 6, no. 10, pp. 1516–1521, Jul. 2012.

[20] O. Saleem, M. Rizwan, K. Mahmood-ul-Hasan, "Self-tuning state-feedback control of a rotary pendulum system using adjustable degree-of-stability design," *Automatika*, vol. 62, no. 1, pp. 84-97, 2021.

[21] L. Hui, L. Xingqiao, L. Jing, "The research of Fuzzy Immune Linear Active Disturbance Rejection Control Strategy for three-motor synchronous system," *Control Eng. Appl. Inform.*, vol. 17, no. 4, pp. 50-58, 2015.

[22] W. Zhou, X. Wang, B. Liu, Y. Chang, J. Liu, W. Zhou, Q. Cai, "A Design of Fuzzy Immune PID Controller for Six-rotor UAV Under Gyroscopic Effect," *IOP Conf. Ser.: Mater. Sci. Eng.*, vol. 631, no. 3, 032045, 2019.

[23] Y. Dai, L. KiDong, L. SukGyu, "A real-time HIL control system on rotary inverted pendulum hardware platform based on double deep Q-network," *Meas Control*, vol. 54, no. 3-4, pp. 417-428, 2021.

[24] S. Balamurugan, P. Venkatesh, "Fuzzy sliding-mode control with low pass filter to reduce chattering effect: an experimental validation on Quanser SRIP," *Sadhana*, vol. 42, no. 10, pp. 1693-1703, Oct. 2017.

[25] K. J. Astom, J. Apkarian, P. Karam, M. Levis, J. Falcon, *Student Workbook: QNET Rotary Inverted Pendulum Trainer for NI ELVIS*. Ontario, Canada: Quanser, 2011.

[26] L. Wang, C. T. Freeman, E. Rogers, D. H. Owens, "Experimentally validated continuous-time repetitive control of non-minimum phase plants with a prescribed degree of stability," *Control Eng. Pract.*, vol. 18, no. 10, pp. 1158–1165, Oct. 2010.

[27] O. Saleem, M. Rizwan, "Performance optimization of LQR-based PID controller for DC-DC buck converter via iterative-learning-tuning of state-weighting matrix," *Int. J. Numer. Model.*, vol. 32, no. 3, e2572, May/Jun 2019.

[28] O. Saleem, K. Mahmood-ul-Hasan, "Hierarchical Adaptive Control of Self-Stabilizing Electromechanical Systems using Artificial-Immune Self-Tuning Mechanism for State Weighting-Factor," *J. Mech. Sci. Technol.*, vol. 35, pp. 1235–1250, Mar. 2021.

[29] O. Saleem, M. Rizwan, F. G. Awan, "Robustification of the State-Space MRAC Law for Under-Actuated Systems via Fuzzy-Immunological Computations," Sci. Progress, vol. 105, no. 3, pp. 1-26, Aug. 2022.

[30] O. Saleem, K. Mahmood-Ul-Hasan, "Indirect Adaptive State-Feedback Control of Rotary Inverted Pendulum Using Self-Mutating Hyperbolic-Functions for Online Cost Variation," *IEEE Access*, vol. 8, pp. 91236-91247, May 2020.